Ni-, Pt- and (Ni/Pt)-doped TiO_2 nanophotocatalysts:

A smart approach for sustainable degradation of Rhodamine B dye

Roberto Pol,[a] Miguel Guerrero,[b] Eva García-Lecina,[c] Ainhoa Altube,[c], Emma Rossinyol,[d] Sebastiano Garroni, [e] Maria Dolors Baró,[b] Josefina Pons,[a] Jordi Sort,*[f] Eva Pellicer[b]*

[a] Departament de Química, Facultat de Ciències, Universitat Autònoma de Barcelona, E-08193 Bellaterra, Spain.

[b] Departament de Física, Facultat de Ciències, Universitat Autònoma de Barcelona, E-08193 Bellaterra, Spain.

[c] Surfaces Division, IK4-CIDETEC, Paseo Miramón, 196, E-20009 San Sebastián, Spain.

[d] Servei de Microscòpia, Universitat Autònoma de Barcelona, E-08193 Bellaterra, Spain.

[e] Dipartimento di Chimica e Farmacia, Università di Sassari and INSTM, Via Vienna 2, I-07100 Sassari, Italy.

[f] Institució Catalana de Recerca i Estudis Avançats (ICREA) and Departament de Física, Universitat Autònoma de Barcelona, E-08193 Bellaterra, Spain.

Corresponding Author

*Miguel.Guerrero@uab.cat

*Jordi.Sort@uab.cat

This is the author's version of a work that was accepted for publication in Applied catalysis B: environmental (Ed. Elsevier). Changes resulting from the publishing process, such as peer review, editing, corrections, structural formatting, and other quality control mechanisms may not be reflected in this document. Changes may have been made to this work since it was submitted for publication. A definitive version was subsequently published in: Pol, Roberto, et al. "Ni-, Pt- and (Ni/Pt)-doped TiO_2 nanophotocatalysts : a smart approach for sustainable degradation of Rhodamine B dye" in Applied catalysis B : environmental, vol. 181 (Feb. 2016), p. 270-8. DOI 10.1016/j.apcatb.2015.08.006

ABSTRACT

Ni (1 wt%)-, Pt (1 wt%)- and [Ni (0.5 wt%) / Pt (0.5 wt%)]-doped TiO_2 nanoporous catalysts have been successfully obtained through a facile two-step hydrothermal route. TiO_2 crystallizes mostly in the anatase phase and acts as a mesoporous matrix. Meanwhile, Ni, Pt and Ni/Pt dopants form small nanoparticles (NPs) (3-95 nm in diameter) which are hosted by the TiO_2 framework. The resulting composites exhibit a rather large surface area, in the range of 186-200 m^2/g. The band gap energy reduces from 3.03 eV for the undoped TiO2 to 2.15 eV for the Pt-loaded TiO_2. As a consequence, absorption expands toward the visible light range. The photodegradation of Rhodamine B dye in aqueous medium has been investigated under UV-Vis light irradiation. The presence of Ni, Pt and Ni/Pt NPs significantly enhances the photocatalytic activity of the material. Furthermore, the Ni-doped TiO_2 shows ferromagnetic behavior at room temperature, which makes its recovery and subsequent fast reutilization possible. Interestingly, this sample also exhibits the best stability upon recycling. Considering all the current challenges in sustainable water remediation, these new photocatalysts could find applications in real environmental contexts in the near future.

KEYWORDS

photocatalyst, nanoporosity, titania, magnetic properties, water remediation

ABBREVIATIONS

NPs, nanoparticles; POPs, persistent organic pollutants; HPO, heterogeneous photocatalytic oxidation; TM, transition metal; HPT, highly porous TiO_2; HRTEM, high resolution transmission electron microscopy; EDX, energy dispersive X-ray; XRD, X-ray diffraction; MAUD, materials analysis using diffraction; BET, Brunauer-Emmett-Teller; BJH, Barrett-Joyner-Halenda; VSM, vibrating sample magnetometer; ICP-OES, inductively coupled plasma - optical emission spectroscopy; RhB, rhodamine B; UV, ultraviolet; Vis, visible; JCPDS, joint committee on powder diffraction standards; fcc, face-centered cubic; S_{bet}, BET surface area; SAED, selected area electron diffraction; M_S, saturation magnetization; DRS, diffuse reflectance spectra; VB, valence band; CB, conduction band; BG, band gap;

1. Introduction

Large amounts of water are currently used in several cleaning and staining processes. Modern industrial activities have left wide-spread hazardous pollution in soil and water across the globe [1]. One of the most troublesome groups of pollutants is persistent organic pollutants (POPs) like dyes, detergents or pesticides due to their water solubility and chemical stability [2-4]. The presence of these colored compounds in the environment causes considerable non-aesthetic pollution and serious health-risk issues [5]. Since conventional wastewater treatments cannot eliminate the majority of these pollutants, powerful methods for the decontamination of dye wastewaters have received increasing attention over the last decade. Ozonation and electrocoagulation are among these methods. However, they consist of multiple steps and are rather costly and time-consuming [6].

Aqueous heterogeneous photocatalytic oxidation (HPO) is considered as one of the greener and cheaper approaches for the removal of POPs. HPO consists in the acceleration of a photoreaction in the presence of a catalyst in water [7]. In other words, it combines water as a green and abundant resource with solar light as an affordable, renewable and clean energy source. HPO involves the breakdown of pollutants into harmless substances while avoiding residues or additional sludge. For these reasons, HPO has received special attention for remediating global water pollution and it is moving fast from the laboratory scale to industrial applications [8,9].

TiO_2 is one of the most studied, environmentally-friendly, photocatalytic materials due to its chemical stability, low toxicity, and light conversion efficiency [10]. Despite these advantages, TiO_2 presents the drawback of limited photocatalytic activity because of its wide

band gap (3.2 eV for anatase phase). Therefore, it requires excitation wavelength in the UV domain ($\lambda < 390$ nm), which limits its practical efficiency. One of the most common approaches to expand the TiO_2 response toward the visible light domain is through doping it with suitable anions (e.g. N, C, S) or cations and transition metal (TM) clusters or nanoparticles (NPs) [11,12].

The controlled doping of TiO_2 with TM species has been the object of several investigations. An enhancement of the catalytic activity of TiO_2 in a number of manifold reactions has been ascribed to the effects induced by the TM at various levels. For example, Mn-Ni doped TiO_2 catalysts showed increased NO reduction to N_2 and offered the possibility to widen the temperature window of the reaction [13]. Also, Nb-doped TiO_2 particles have been studied as electrocatalysts for the oxygen reduction reaction under acidic conditions [14].

Among the TMNPs available to be dispersed on high-surface area TiO_2 for photocatalytic purposes, those made of Pt hold a privileged position [15-17]. In general, the resulting nanocomposite benefits from the catalytic activity of the TMNPs and the intrinsic photocatalytic activity of TiO_2. If the TMNPs possess magnetic properties (e.g. Ni, Co, Fe), then recovery and recycling of the catalyst becomes feasible under the application of a magnetic field. This poses some advantages compared to cross-flow filtration or centrifugation processes [18], since the recovery of a catalyst using magnetic fields is much cheaper and faster.

In this work, nickel, platinum and nickel/platinum-doped TiO_2 porous nanophotocatalysts have been successfully obtained through a easy two-step hydrothermal route. The morphology, crystallographic structure of the composite constituents, and eventual magnetic properties of the material have been investigated. Furthermore, the degradation kinetics of Rhodamine B (RhB) dye under ultraviolet-visible light irradiation has been assessed. ~~Our results indicate that the~~

~~doped samples exhibit higher photocatalytic activity than pure TiO_2.~~ RhB is one of the most common xanthene dyes used as a colorant in the textile industry. It is highly water soluble and presents a good stability as dye laser material. Nowadays, its use has been forbidden due to the potentially toxic and carcinogenic properties of RhB. Thus, the photodegradation of this organic compound is important with regard to the purification of dye effluents. ~~Furthermore, the Ni-containing catalysts can be easily recovered from the media using weak magnetic fields, making them a smart approach for sustainable water remediation.~~

2. Materials and methods

2.1. Sample preparation

All chemicals were commercially available and used without further purification. Titanium (lV) butoxide (97%), 1-butanol (99.9%), nitric acid (69%), chloroplatinic acid hexahydrate ($H_2PtCl_6•6H_2O$) (37.5% Pt basis) and nickel (II) nitrate hexahydrate ($Ni(NO_3)_2•6H_2O$) (20.19% Ni basis) were purchased from Sigma Aldrich. Pluronic P123 was provided by BASF.

Highly porous TiO_2 (denoted as 'HPT') sample was prepared by sol-gel hydrothermal method. First, 7 mL of titanium butoxide (VI) dissolved in 40 mL of 1-butanol was added dropwise to 60 mL of distilled water at pH = 2 (adjusted with nitric acid). After continuous stirring of the reaction mixture for 20 h, the resultant suspension was subjected to a hydrothermal treatment in a plastic flask at 80 ºC for 2 h. Afterwards, 2.5 g of Pluronic P123 triblock copolymer was dissolved in 40 mL of distilled water and the solution was added dropwise to the titanium (VI) butoxide solution, which had been previously cooled down to 45 ºC. Then the mixture was stirred at this temperature for 2 h followed by a second hydrothermal treatment in a

plastic flask at 80 ºC for 20 h. The resultant powder was recovered by evaporation at 60 ºC. Finally, the titania product was obtained by calcination in a furnace at 450 ºC for 4 h in air, by which the P123 was also removed.

Nickel, platinum and nickel/platinum-doped TiO_2 (denoted as 'Ni/HPT', 'Pt/HPT' and 'Ni/Pt/HPT', respectively) were prepared following a similar procedure to that of pure TiO_2. A P123-titanium (VI) butoxide mixture was obtained as described above prior to the doping step. To dope TiO_2 with Ni, Pt and bimetallic Ni/Pt NPs, a solution containing the metal salts (nickel (II) nitrate hexahydrate, chloroplatinic acid hexahydrate or chloroplatinic acid hexahydrate + nickel (II) nitrate hexahydrate) in 10 mL of distilled water was added dropwise to the P123-titanium (VI) butoxide mixture at 80 ºC. Unless otherwise stated, the loading amounts were 1 wt% for both Ni/HPT and Pt/HPT samples and 0.5 wt%/0.5 wt% for the Ni/Pt/HPT sample. The mixture was subjected to 30 min sonication in order to achieve good dispersion of the precursors. The resultant powder was recovered by evaporation at 60 ºC. This was followed by a thermal treatment in a furnace at 450 ºC under H_2 atmosphere for 4 h in order to obtain the doped nanocomposites.

2.2. Characterization

High resolution transmission electron microscopy (HRTEM) was performed on a Jeol-JEM 2011 system operated at 200 kV and equipped with energy dispersive X-ray (EDX) detector. Scanning electron microscopy (SEM) observations were done using a Merlin Zeiss microscope operated at 2 kV. Samples for HRTEM were prepared by dispersing a small amount of powder in ethanol (96%) followed by sonication. A holey carbon grid was then soaked into the suspension and allowed to dry in air. The size distribution of Ni and Pt NPs was determined

via manual analysis of enlarged micrographs. Around 100 particles were counted in order to obtain statically meaningful size distributions and the mean diameter. Wide-angle X-ray diffraction (XRD) patterns were collected on a Philips X'Pert diffractometer in the 20º – 80° 2θ range (step size = 0.03°, step time = 10 s) using CuKα radiation. The structural parameters (phase percentage, crystallite size and cell parameters) were determined using the "Materials Analysis Using Diffraction" (MAUD) Rietveld refinement software [19,20].

N_2 sorption isotherms were measured on a Sorptomatic 1990 and the data were analyzed according to Brunauer-Emmett-Teller (BET) and Barrett-Joyner-Halenda (BJH) methods [21]. Around 800 mg of powder were charged in a quartz tube and then degassed under high vacuum ($1x10^{-3}$ bar) at 250 °C for 24 h to remove the solvent. Room temperature hysteresis loops were collected using a vibrating sample magnetometer (VSM) from Oxford Instruments, with a maximum applied magnetic field of 1 T. Inductively coupled plasma - optical emission spectroscopy (ICP-OES) was carried out on a Perkin-Elmer Optima 4300DV model. 2-5 mg of powder were digested in aqua regia and concentrated hydrofluoric acid (HF) solution at 200 ºC for 8-10 min on a CEM model MARS microwave oven.

2.3. Evaluation of photocatalytic activity

The photocatalytic activity of the powder samples was evaluated by decolorization of a 10 ppm RhB aqueous solution (Alfa Aesar, 98%, used without further treatment). Solutions were prepared by adding 0.3 g L^{-1} of the catalyst to 10 mL of the RhB solution. A blank RhB solution (without catalyst) was used as a control test. The reaction cells were placed in a SwiftCure IB irradiation cabin equipped with a mercury lamp. Suitable cut-off filters were used to limit the wavelength radiation and avoid direct photolysis of the dye (ISO 10678:2010 standard). The average light intensity used was 220 W and the wavelength ranged from 300 to 500 nm, thus

covering part of ultraviolet (UV) (300-400 nm) and visible (Vis) (400-700 nm) regions. The photocatalytic experiments were conducted under continuous magnetic stirring at a constant temperature of 25 ºC.

Aliquots were withdrawn regularly at time intervals of 0, 15, 30, 60, 120, and 180 min from the reaction. The supernatant solutions were then tested with a UV-Vis spectrophotometer (Shimadzu UV-1603) by measuring absorption spectra of RhB (λ= 554 nm) as a function of the irradiation time. Photocatalytic activity of the catalysts was calculated as (C/C_0), where C_0 is the absorbance of the test solution of RhB before irradiation and C is the absorbance of RhB after irradiation. The optical diffuse reflectance spectra were measured at room temperature using the same UV-Vis instrument equipped with an integrating sphere attachment and using NaF as reference. In order to investigate the reusability of the photocatalysts, five consecutive cycles were conducted. After each cycle, the photocatalytic material was centrifuged, collected and dispersed in a fresh RhB aqueous solution.

3. Results and discussion

3.1. Morphological and structural characterization

In scheme 1 is presented the synthesis route toward HPT, Ni/HPT, Pt/HPT and Ni/Pt/HPT samples. The total dopant metal amount was kept at 1 wt% in the synthesis. The actual Pt and Ni amounts determined by ICP-OES are shown in Supplementary Data (Table S1). The results indicate that there is no significant difference between the nominal and the actual dopant metal percentage in the nanocomposites.

The crystallographic structure of the different samples was studied by XRD (Figure 1). Broad reflections ascribed to TiO_2 were observed for all samples, indicating its nanocrystalline

nature. The most predominant phase in the diffractogram of non-doped TiO_2 sample (HPT) is anatase (tetragonal phase) (JCPDS no. 84-1286). Namely, the peaks at 25.3º, 37.8º and 48.0º correspond to the (101), (004) and (200) crystal planes, respectively, of TiO_2-anatase structure. The brookite phase is also present, as revealed by the characteristic reflection of (211) at 2θ = 30.7º. Besides the characteristic diffraction peaks of anatase and brookite phases, the diffractogram of Ni-doped TiO_2 sample (Ni/HPT) exhibits two reflections at 44.6º and 52.0º that match the positions of (111) and (200), respectively, of face-centered cubic (fcc) Ni. Likewise, the diffractogram of Pt-doped TiO_2 (Pt/HPT) shows two reflections at 39.6º and 46.2º ascribed to (111) and (200) planes, respectively, of fcc Pt. The bi-doped sample (Ni/Pt/HPT) does not present any reflections ascribed to Ni and/or Pt due to the lower amounts of both dopant metals (0.5 wt%), which fall below the sensitivity limit of the XRD technique (1-2 wt%).

Anatase and brookite phase percentages, as determined by Rietveld refinement of the full XRD patterns, as well as the cell parameter values and average crystallite size for anatase phase are listed in Table S2. All samples show lower *c* parameter than that of tabulated anatase (9.513 Å, JCPDS no. 84-1286). This could be attributed to the occurrence of unit cell shrinkage during the calcination process. Several factors like titania precursor [22], synthetic method [23] and calcination conditions [24] are known to determine the TiO_2 phase –rutile, anatase or brookite– and their relative proportion. Besides, samples show an average crystallite size in the range of 10-12 nm, in agreement with previous reports [25-28].

Figure 2 shows the N_2 adsorption−desorption isotherms and the pore size distributions of all samples. A type IV isotherm characteristic of mesoporous materials is observed in all cases [29]. The adsorption branch exhibits three distinct regions corresponding to a monolayer-multilayer adsorption, multilayer adsorption on the outer particle surfaces and capillary

condensation at relative pressures in the range from 0.6 to 0.9, for all the isotherms. H_2-type hysteresis loop is observed, typical of samples with ink-bottle shaped pores and interconnecting channels. The powders showed a BET surface area (S_{bet}) of 186-200 m^2/g, with no significant differences among non-doped and doped TiO_2, in agreement with the results of Di Paola et al [30] (Table 1). Either unimodal or bimodal pore size distributions (Figure 2, insets), with a maximum pore diameter between 7.8 and 10.9 nm and a cumulative pore volume between 0.456 and 0.572 cm^3/g, were obtained, similar to the values reported by E. Masolo et al. [31] A narrower pore distribution was noticed for Pt/HPT sample (Figure 2c, inset). It is conjectured that the narrower pore distribution in the Pt/HPT sample is mainly due to the very small size of the nucleated Pt NPs in comparison to that of the Ni ones (3 nm vs. 95 nm as it will be shown later). TiO_2 matrix formation is probably less disturbed when smaller NPs are accommodated within the network. As a result, the formation of the TiO_2 matrix becomes less perturbed when Pt is present and a narrower pore distribution is achieved. Interestingly, all doped samples exhibit a higher average pore diameter than non-doped TiO_2 sample.

To gain further structural information on the samples, TEM and HRTEM analyses were performed. HPT is highly porous and crystalline (Figure 3a and 3b). The corresponding selected area electron diffraction (SAED) pattern (Figure 3c) shows continuous rings indicating the existence of tiny crystals. Indexing of the primary rings is consistent with the existence of anatase ((101), (004) and (200) crystal planes) and brookite phases ((211) reflection) in agreement with XRD results. The most intense ring corresponds to an interplanar distance of 3.5 Å, which matches the *d* spacing of (101) anatase. HRTEM images of Ni/HPT and Pt/HPT nanocomposites (Figure 3d and 3e) show well dispersed Ni and Pt rounded NPs, respectively. The average size of the Ni NPs in Ni/HPT sample is much larger than that of Pt NPs in Pt/HPT

sample (95 nm and 3 nm, respectively) (Figure S1). This difference in size could originate from the ability of Pt and Ni precursors to diffuse within the TiO_2 matrix. Although no bibliographic data of diffusion coefficients for Pt and Ni cations onto TiO_2 surfaces exist, it is believed that the coefficient diffusion of Pt cation is higher than that of Ni cation. The higher the diffusion coefficient, the easier the atoms can diffuse onto the TiO_2 to ultimately give rise to NPs of larger size. The inset in Figure 3d shows a SAED pattern of the Ni/HPT sample focused on a Ni NP, in which it is possible to distinguish a clear diffraction spot array whose *d* spacing is 2.02 Å. Such *d* spacing corresponds to (111) fcc Ni, which appears superimposed to the lattice rings of anatase. Interestingly, Ni and Pt NPs are also well dispersed in the bi-doped Ni/Pt/HPT nanocomposite (Figure 3f). Notice that Ni and Pt do not form a core-shell structure or an alloy but rather they have nucleated independently, rendering individual single-phase NPs.

SEM imaging was used to study the surface morphology as well as the porosity of the different nanocomposites. Figure 4 shows SEM secondary electron images taken at different magnifications of the HPT sample, for which a large porosity is evident, in concordance with BET analyses. Porosity was preserved in the doped HPT samples (e.g. Ni/HPT in Figure S2).

3.2. Magnetic and optical properties

The magnetic properties of the Ni-containing catalysts (i.e., Ni/HPT and Ni/Pt/HPT) were investigated using a vibrating sample magnetometer at room temperature (Figure 5). The Ni/HPT sample exhibits a saturation magnetization (M_S) of 0.4 emu g^{-1} and a coercivity of around 80 Oe. Interestingly, although the M_S of the Ni/HPT powder is not high, it is large enough for the powder to become attracted by a circular NdFeB magnet (2500 Oe) of about 1 cm in diameter magnet when it is brought near the sample (inset of Figure 5). Almost all photocatalyst (99 wt.%)

it is recovered after each cycle using this magnetic separation procedure, as verified from values of sample weight before and after the degradation process. On the other hand, the Ni/Pt//HPT sample does not show a ferromagnetic behavior (i.e., no clear hysteresis loop).

UV-Vis diffuse reflectance spectra (DRS) were carried out prior to the assessment of the photo-degradability performance of each catalyst. It is known that the optical properties of a photocatalyst and its catalytic performance are closely related [32]. HPT sample presents strong absorption only at wavelengths below 400 nm. Therefore, it shows photoabsorption only in the UV domain (Figure 6). On the other hand, the spectra of doped samples (Ni/HPT, Pt/HPT and Ni/Pt/HPT) show a similar response in the UV domain and also absorption within the visible domain. In other words, the absorption spectrum expands into the visible range. This result can be attributed to the excitation of 3d (for Ni) and/or 5d (for Pt) electrons from the transition metal valence band (VB) to the TiO_2 conduction band (CB). [33]

The band gap (BG) energies (Table 2) were determined using the equation:

$$E_g = hc_0/\lambda_g \qquad (1)$$

where E_g is the energy of the band gap in eV, h is the Planck's constant (6.626×10^{-34} Js), c_0 is the speed of light in vacuum (3×10^8 m/s) and λ_g is the value obtained measuring the intersection of the tangent of the absorption edge with the x-axis [34]. The absorption edge of HPT was noted at 408 nm, corresponding to a BG energy value of 3.03 eV. Conversely, Pt/HPT and Ni/HPT and Ni/Pt/HPT nanocomposites all possess smaller BG values (2.69-2.15 eV, Table 2).

3.3. Photocatalytic Activity

The photocatalytic performances of the catalysts were investigated by following the decomposition of Rhodamine B (RhB) in an aqueous solution under irradiation with a mercury

lamp (320-500 nm). No significant degradation of RhB was observed in the absence of any photocatalyst, which was taken as a reference (blank).

As shown in Figure 7a, the concentration of RhB decreases linearly with time in the presence of the HPT sample, reaching a removal ratio of 39% after exposure for 180 min. The removal ratio of Pt/HPT, Ni/HPT and Ni/Pt/HPT were 63, 57 and 54 %, respectively. The results show that there is an enhancement in the photodegradability of RhB when Ni or Pt NPs (or combinations of both) are loaded into TiO_2. Previous works in the literature indicate that the photocatalytic oxidation of different dyes using TiO_2 as a catalyst follow the Langmuir-Hinshelwood kinetics model [35-37]. For very diluted catalyst suspensions (millimolar), though, the reaction can be described as a pseudo-first-order equation. This applies to our case (Figure 7b), for which the ln (C/C_0) versus time follows a linear relationship. The slope corresponds to the apparent first-order rate constant (k, min^{-1}). The rate constants values (Table 2) show that Ni- and Pt-doped nanocomposites outperform HPT sample. Pt/HPT, with a BG energy value of 2.15 eV, presents the highest rate constant, 0.0053 min^{-1}. ~~This is not surprising bearing in mind that Pt is the top-ranked catalyst metal~~. Meanwhile, Ni/HPT sample shows a slightly lower *k* value (0.0046 min^{-1}). Curiously, the corresponding *k* value for the bi-doped sample is lower than those of the single-doped TiO_2 catalysts. In spite of it, it is envisaged that having two different types of NPs physically separated but in the same support can be advantageous in certain cases. For example, two different reactions could be simultaneously catalyzed by taking advantage of the joint presence of Pt and Ni in the matrix. The rate constant of Pt/HPT sample is higher than that observed in the degradation of RhB using core(metal)-shell(TiO_2) nanocomposites (e.g. Pt, k = 0.0013 min^{-1}) synthesized via a hydrothermal treatment with noble metal colloid particles [38]. Our results are also in good agreement with those previously reported by Chen et al. [39], who

also observed an increase in the rate constant towards the degradation of *o*-cresol upon doping TiO_2 with Pt.

In order to further explore the influence of the dopant metal concentration on the photodegradation of RhB, two additional samples were prepared: Ni(3 wt%)/HPT and Pt(3 wt%)/HPT. The Ni and Pt particle size distributions are shown in Figure S1. Notice that the average particle size is in both cases reduced as compared to the 1 wt% concentration. Additionally, the corresponding XRD patterns are also shown in Figure S3. The RhB removal ratio of Ni(3 wt%)/HPT and Pt(3 wt%)/HPT were 39 and 38%, respectively, almost the same removal ratio of non-doped HPT sample (Figure S4). Accordingly, there is a decrease of the photocatalytic efficiency when the concentration of dopant is exceedingly large. This can be explained by taking two scenarios into account: (1) the TMNNPs excess at the surface of TiO_2 decrease the charge carrier space distance (CCSD) via efficiently trapping photoelectrons and therefore increase recombination [40]; (2) a fraction of the active sites become 'covered' or 'shaded' so that the available space on the semiconductor for pollutant adsorption and light absorption is decreased, thereby reducing photodegradation efficiency [41]. Our results are in agreement with those of Dhabbe et al. [42] and Arabatzis et al. [43]. The former observed an enhancement of the photocatalytic performance upon increasing the content of Ag in N-doped TiO_2 nanocomposites until a maximum loading of 1 g/dm^3. The latter pointed out an enhancement of the photocatalytic performance towards methyl orange degradation with an increase of the Au content in TiO_2 thin films till a maximum of 0.8 $\mu g/cm^2$. In both cases, the catalytic activity diminished with further increase of the dopant concentration. Nevertheless, it is worth noticing that the Ni(3 wt%)/HPT sample exhibits a higher M_S value (0.87 emu g^{-1}), as

expected for a larger Ni amount. Therefore, in those cases where a larger M_S is required to recover the catalyst, this sample still has the potential to be used.

The recyclability of the doped TiO_2 nanocomposites was tested for 5 photodegradation cycles of 60 min each (Figure 8). The results show that the photocatalytic activity begins to fairly decline in the fourth cycle. This effect could be due to the presence of radicals with high reduction potentials that might cause partial oxidation of the TMNPs. It should be noted that the decrease of the photocatalytic activity is less pronounced in the Ni/HPT sample (Figure 8, green), making it the most suitable catalyst in terms of reusability for the decomposition of POPs. The reason why Ni/HPT is more durable than Pt/HPT might arise from the distinct mean size of Ni and Pt NPs (95 nm and 3 nm, respectively). Even though Pt is less prone to oxidation, the size-dependence reactivity effect of the NPs cannot be ruled out. In the case of Pt a larger fraction of surface atoms would be exposed to the medium and, hence the photocatalytic activity would decline earlier for the Pt/HPT sample.

Regarding the mechanism (Figure 9a) behind the decomposition of RhB under UV-vis irradiation, it is conjectured that an electron (e_{CB}^-) and a hole (h_{VB}^+) are produced (Figure 9b,i). On the one hand, e_{CB}^- can reduce O_2 to form superoxide radical anion (Figure 9b,ii). Simultanely, h_{VB}^+ can oxidize H_2O to form hydroxil radicals (Figure 9b,iii). Finally, RhB mineralization occurs (Figure 9b,iv). For optimum TMNPs content and size (i.e. 1 wt%), reaction (ii) would be favored. In this case, the CCSD is thought to increase. The band gap energy is reduced and, as a consequence, the absorption band extends toward the visible light domain. The fact that the Pt/HPT outperforms Ni/HPT can be attributed to a higher electron affinity and suitable work function of Pt metal, so that a better contact with TiO_2 forms [40]. On the contrary, for

exceedingly large contents, recombination of charge carries competes with (ii) due to the decrease in the CCSD and/or the partial blocking of the available active for light absorption.

4. Conclusions

Ni-, Pt- and Ni/Pt-loaded TiO_2 nanophotocatalysts have been successfully prepared via a two-step hydrothermal route. The powders show a large porosity provided by the TiO_2 compound. The presence of Ni and Pt NPs within the TiO_2 matrix does not compromise the porosity, which remains large. TEM/HRTEM images reveal a homogenous distribution of the TMNPs within the sample powders, although the average NP size is different (that of Pt NPs is smaller). The photocalytic activity of the nanocomposites outperforms that of non-doped TiO_2 synthesized following the same procedure. Higher degradation rates of Rhodamine B dye under UV-vis light irradiation are achieved (63% for Pt-, 57% for Ni and 54% for Ni/Pt-doped TiO_2 against 39% for undoped TiO_2). Furthermore, the Ni-doped TiO_2 sample presents sufficiently large M_S values to allow its fast recovery from the media using relatively weak magnetic fields and subsequent reuse. The relative dye degradation keeps fairly constant up to the 4^{th} cycle but starts to decrease onwards. Further work is in progress to elucidate the reasons behind such slight decrease in the photocatalytic activity, especially for the Pt-containing catalyts. Remarkably, an increase in the amount of loaded NPs does not bring an enhancement of the photocatalytic activity. Therefore, the tested dopant concentration (1 wt%) can be regarded as optimal. Considering the simplicity of the fabrication process and the attributes of these nanophotocatalysts, we expect that these materials could find uses in sustainable water remediation processes in the near future.

Figure captions

Figure 1. XRD data of HPT, Ni/HPT, Pt/HPT and Pt/Ni/HPT samples.

Figure 2. N_2 adsorption (blue dots)-desorption (red dots) isotherms of (a) HPT, (b) Ni/HPT, (c) Pt/HPT and (d) Ni/Pt/HPT samples and their respective pore size distributions (insets).

Figure 3. TEM and HRTEM images of (a, b) HPT at different magnifications and (c) the corresponding SAED pattern; B means brookite phase. (d) TEM image of Ni/HPT (the SAED is shown in the inset), (e) HRTEM image of Pt/HPT, (f) TEM image of Ni/Pt/HPT.

Figure 4. (a-c) On-top SEM images at different magnification of the non-doped HPT sample.

Figure 5. Room-temperature magnetic hysteresis loops of Ni/HPT and Ni/Pt/HPT samples.

Figure 6. UV-Vis absorption spectra of HPT, Ni/HPT, Pt/HPT and Ni/Pt/HPT samples.

Figure 7. (a) C/C_0 vs time plot showing the decrease of the dye concentration. (b) $\ln(C/C_0)$ of RhB vs time.

Figure 8. Relative RhB degradation as a function of the number of cycles.

Figure 9. Scheme of the proposed photochemical charge promoted separation.

Figure 1.

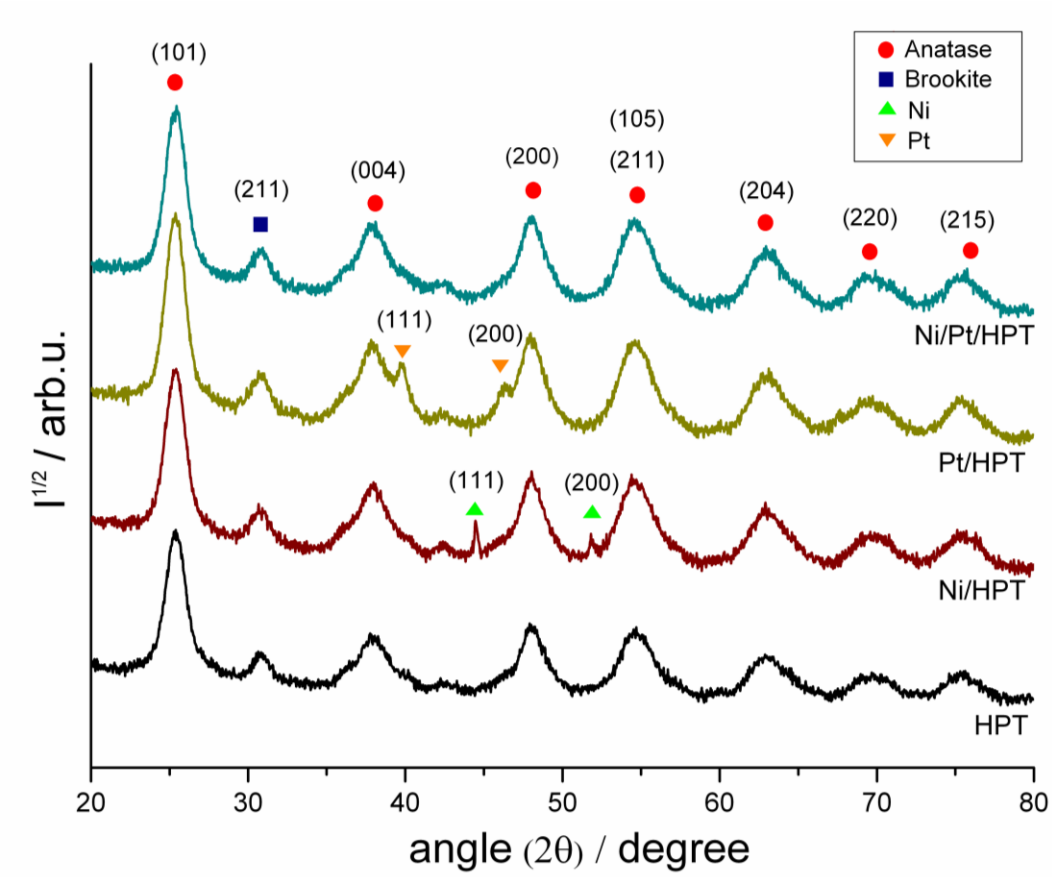
Anatase
Brookite
Ni
Pt
(101)
(211)
(004)
(200)
(105)
(211)
(204)
(220)
(215)
(111)
(200)
(111)
(200)
Ni/Pt/HPT
Pt/HPT
Ni/HPT
HPT
I^1/2 / arb.u.
20
30
40
50
60
70
80
angle (2θ) / degree

Figure 2.

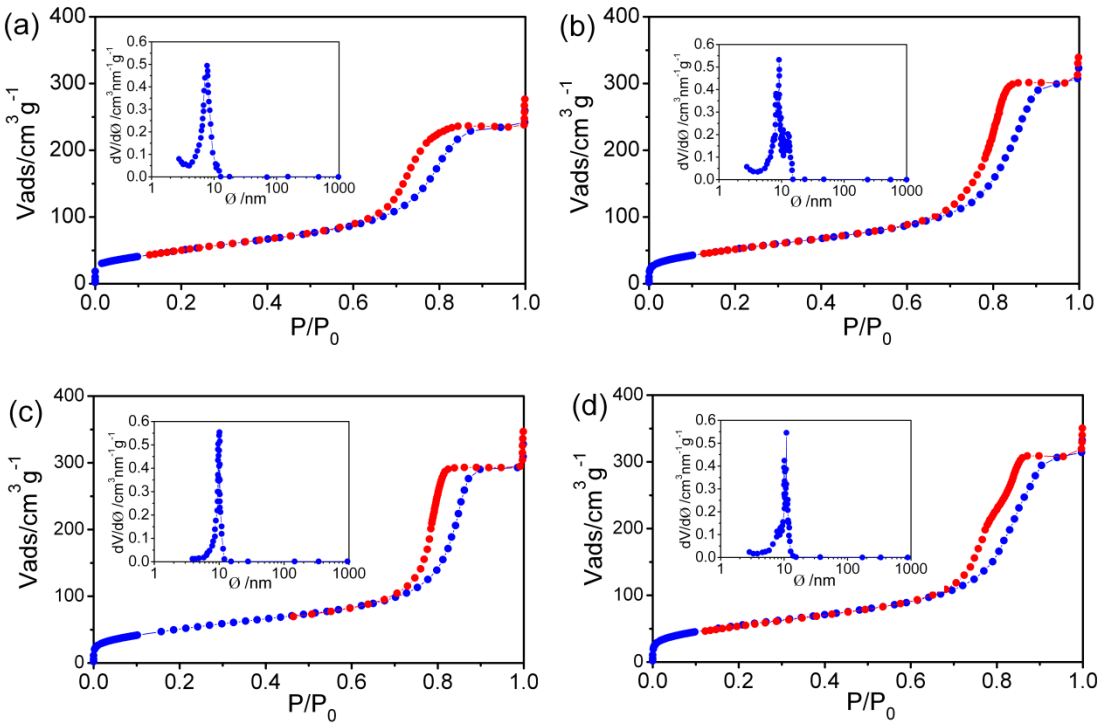

Figure 3.

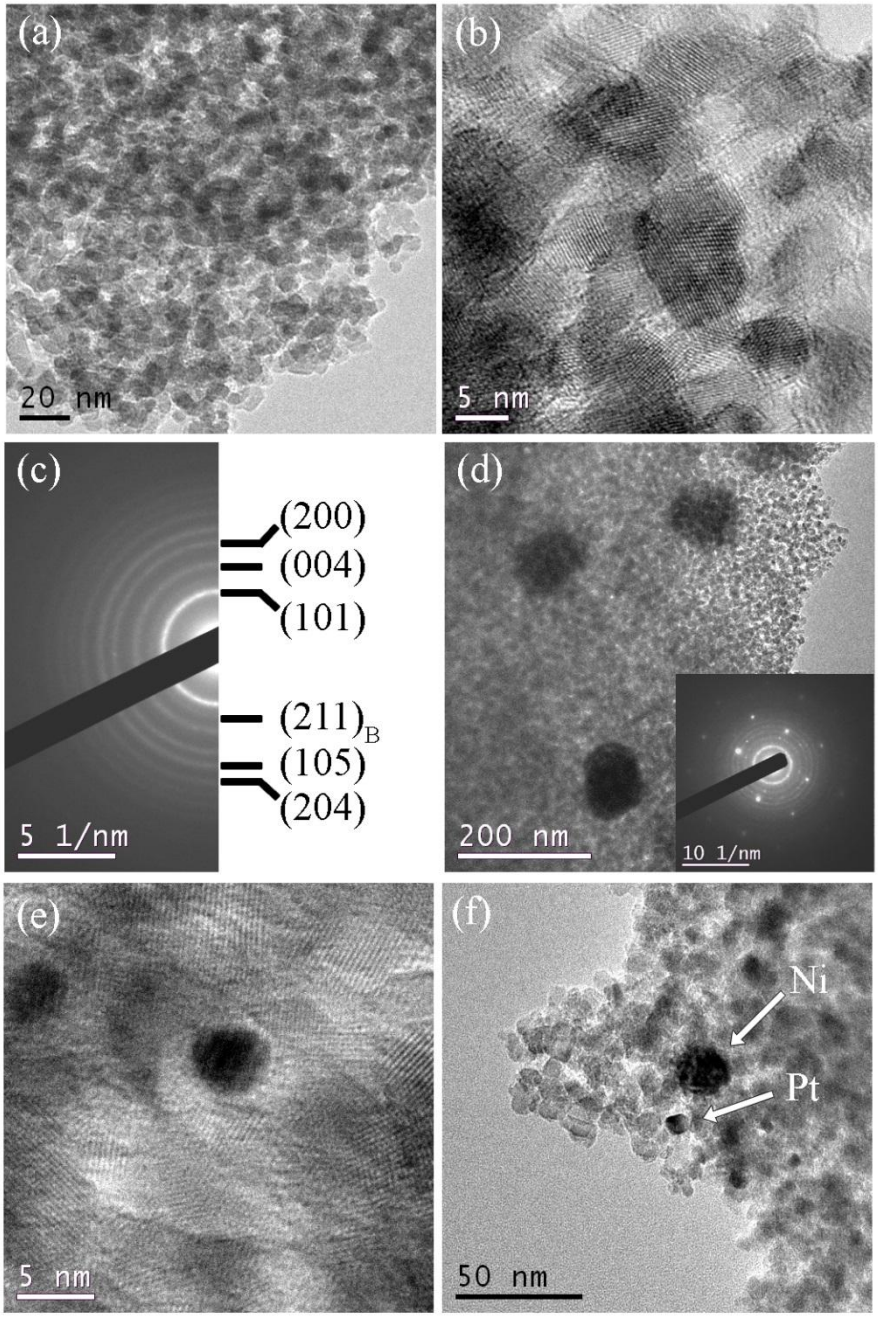
(a)
20 nm
(b)
5 nm
(c)
(200)
(004)
(101)
(211)B
(105)
(204)
5 1/nm
(d)
200 nm
10 1/nm
(e)
5 nm
(f)
Ni
Pt
50 nm

Figure 4.

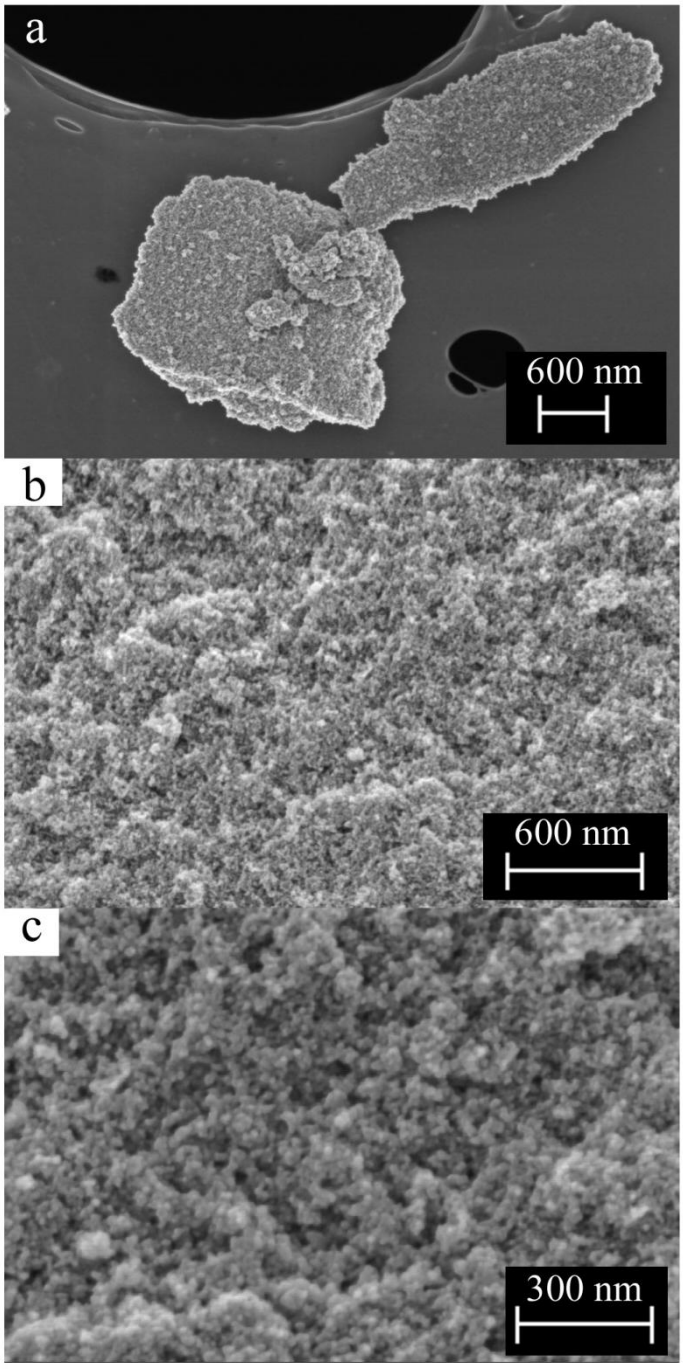

Figure 5.

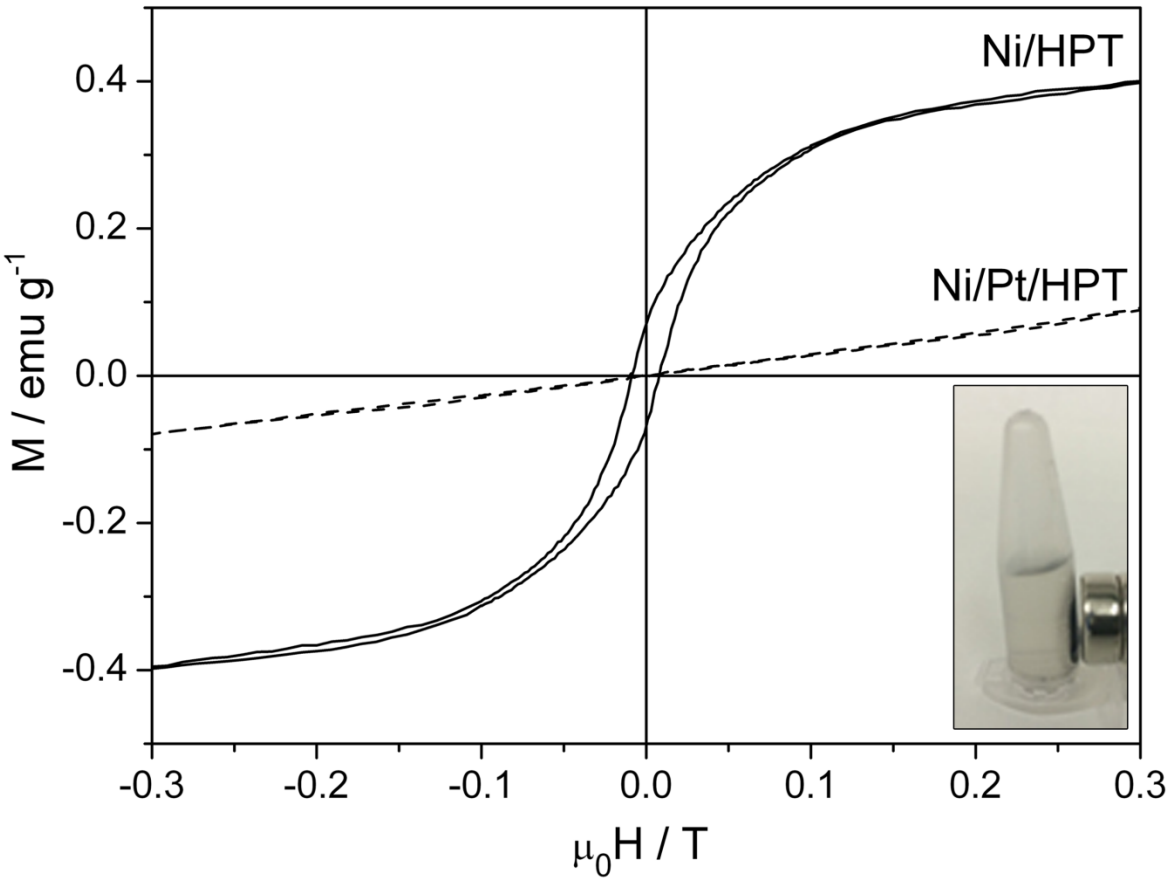

Figure 6.

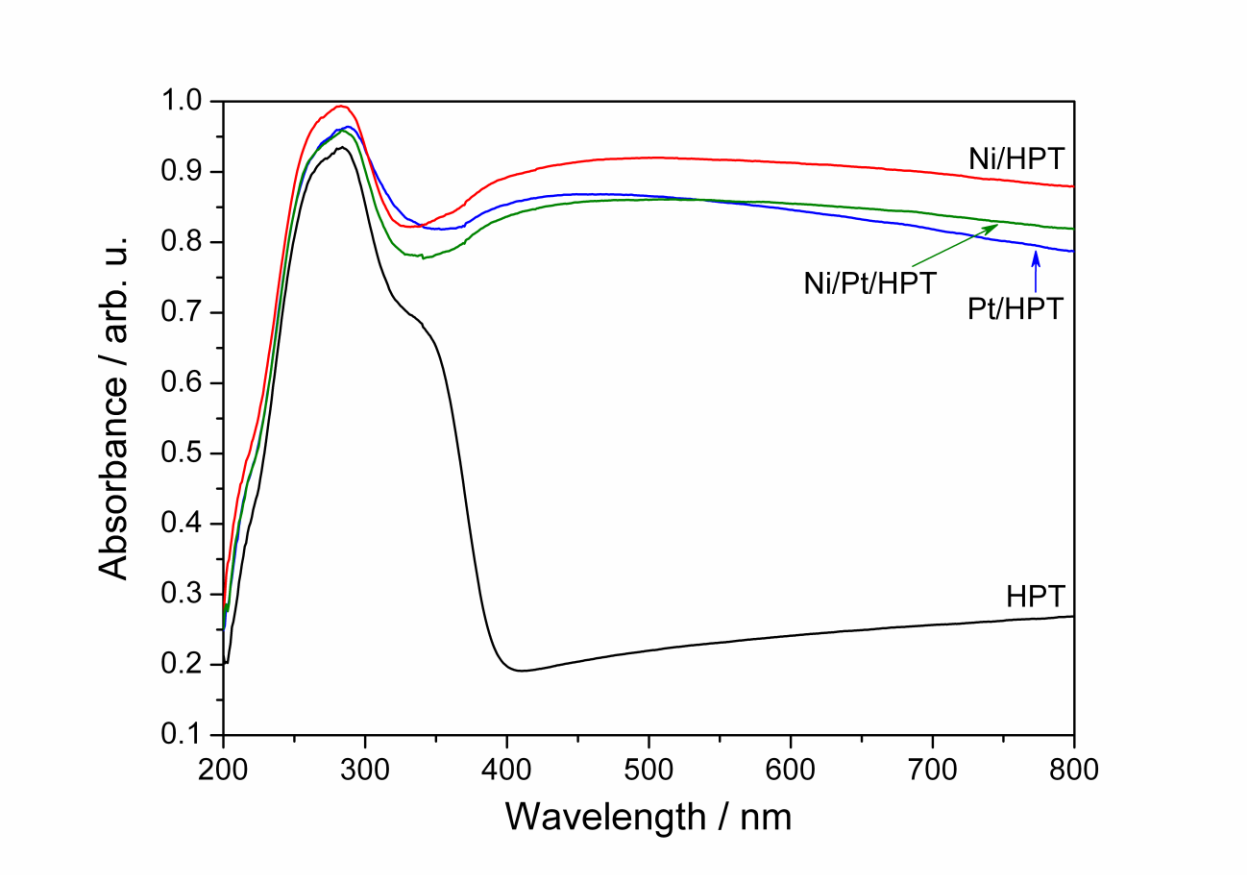
Absorbance / arb. u.
Wavelength / nm
1.0
0.9
0.8
0.7
0.6
0.5
0.4
0.3
0.2
0.1
200
300
400
500
600
700
800
Ni/HPT
Ni/Pt/HPT
Pt/HPT
HPT

Figure 7.

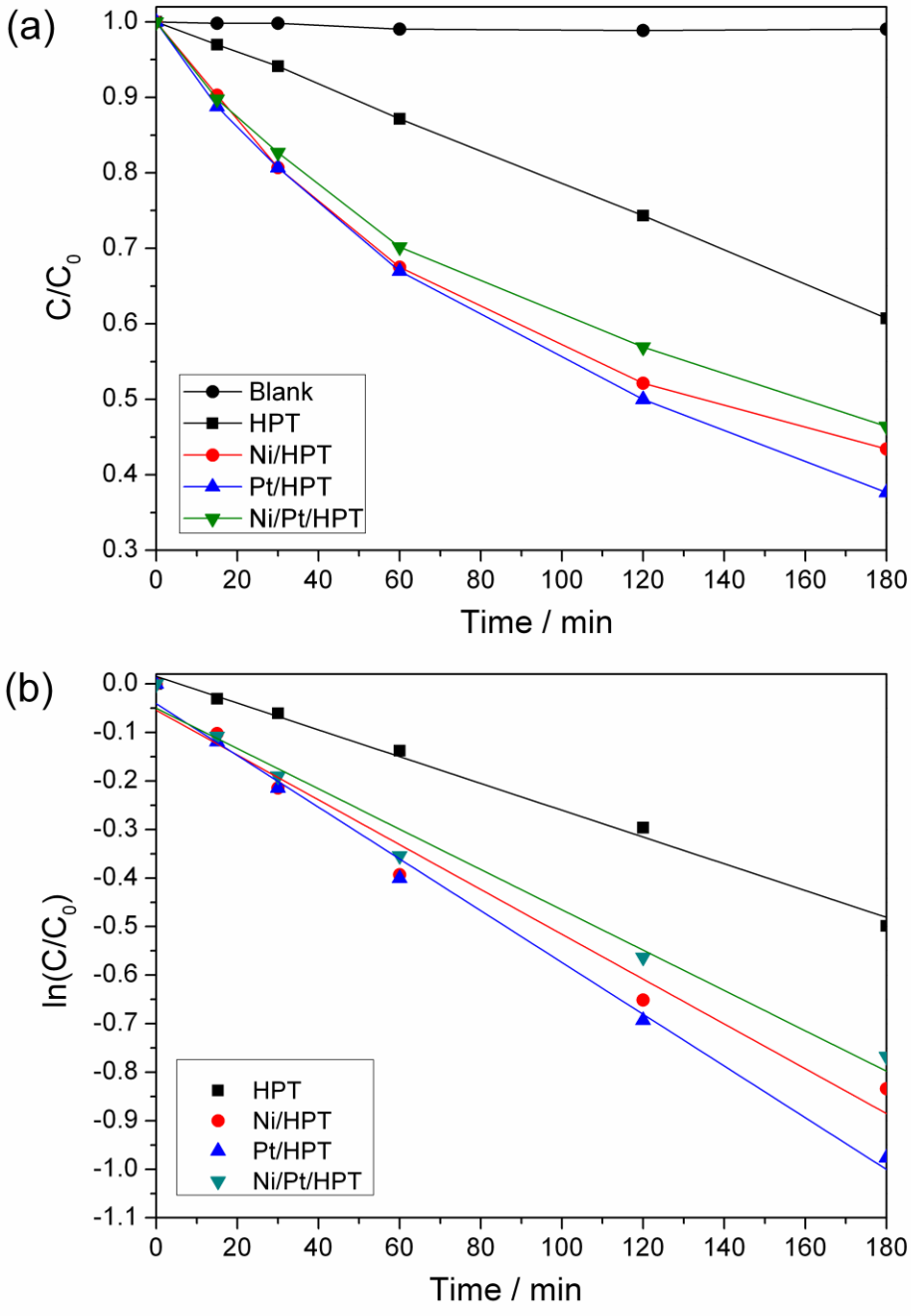
(a)
C/C0
Time / min
Blank
HPT
Ni/HPT
Pt/HPT
Ni/Pt/HPT
(b)
ln(C/C0)
Time / min
HPT
Ni/HPT
Pt/HPT
Ni/Pt/HPT

Figure 8.

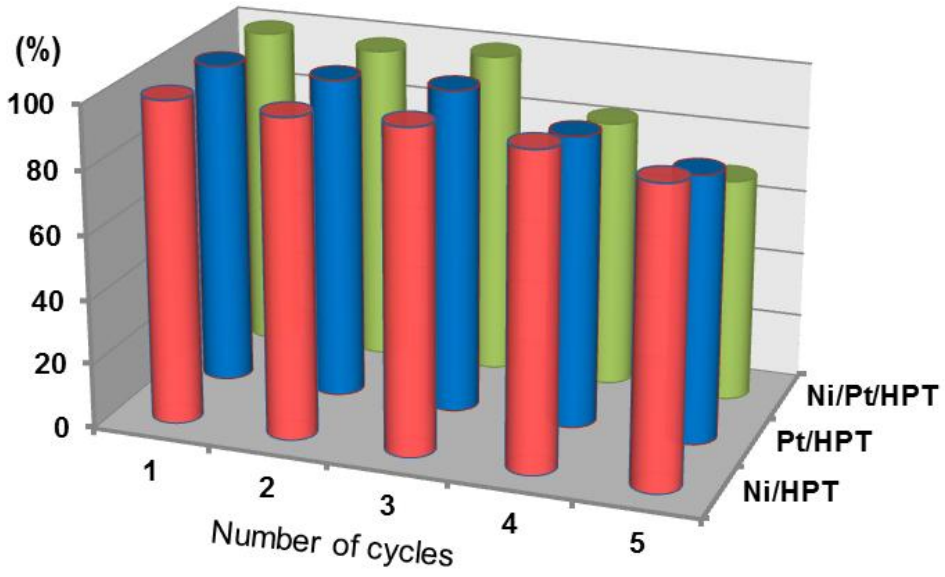

Figure 9.

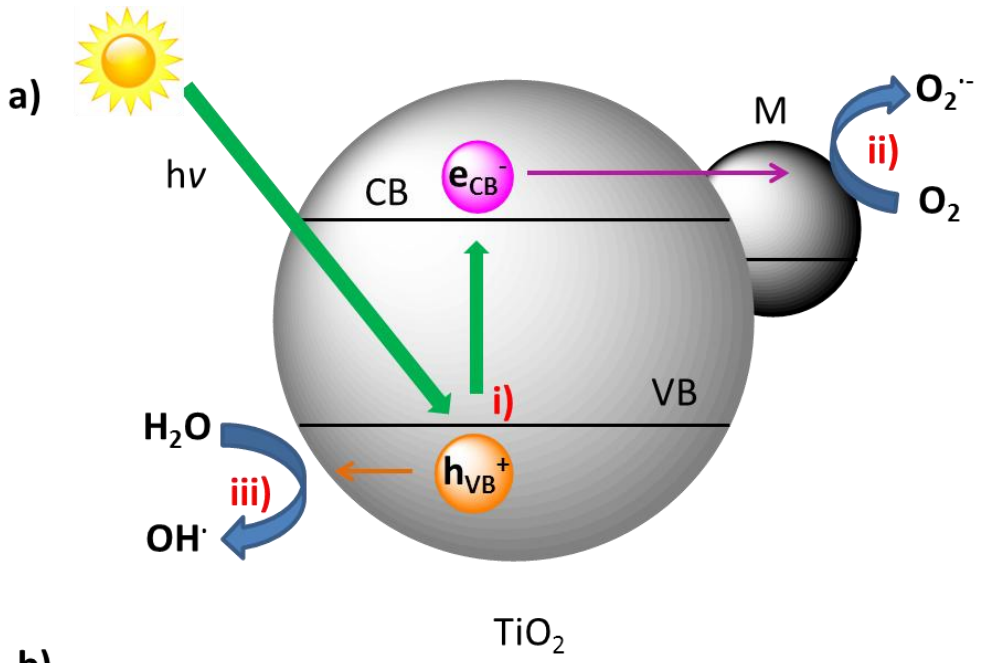

b)

i) $M\text{-}TiO_2 \xrightarrow{h\nu} M(e_{CB}^-)\text{-}TiO_2(h_{VB}^+)$

ii) $M(e_{CB}^-) \xrightarrow{O_2} O_2^{\cdot-}$

iii) $TiO_2(h_{VB}^+) \xrightarrow{H_2O} H^+ + OH^{\cdot}$

iv) $RhB \xrightarrow{O_2^{\cdot-}/OH^{\cdot}} CO_2 + H_2O + \ldots$

Scheme 1. Synthesis of undoped TiO_2 (HPT) and Ni-, Pt- and Ni/Pt-doped TiO_2 nanophotocatalysts (Ni/HPT, Pt/HPT and Ni/Pt/HPT, respectively).

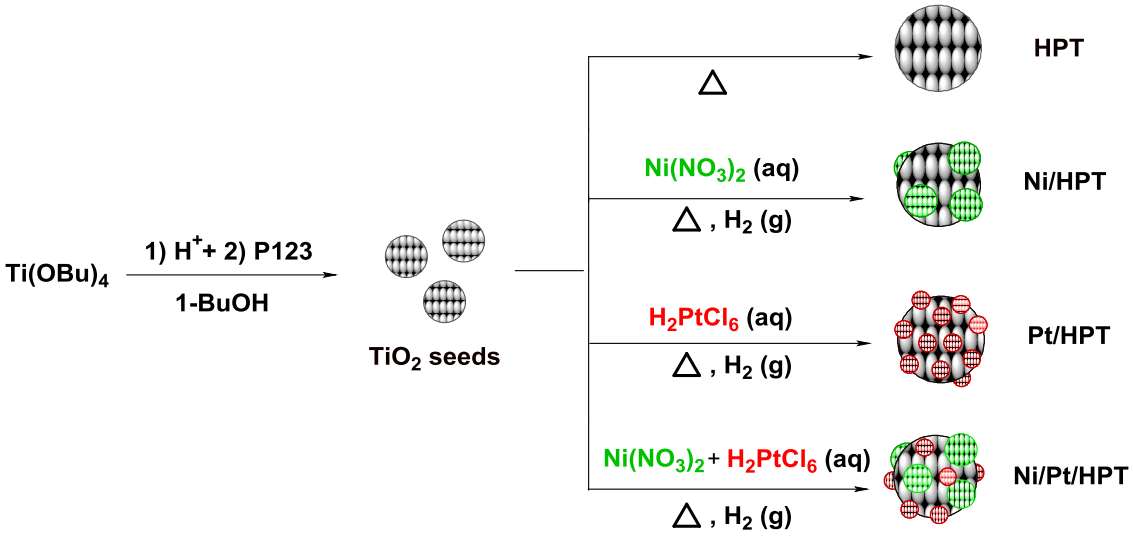

Table 1. Textural parameters determined by BET of HPT, Ni/HPT, Pt/HPT and Ni/Pt/HPT powders.

Samples	**S_{bet} (±5 m^2/g)**	**Maximum pore diameter (±0.2 nm)**	**Average pore diameter (±0.2 nm)**	**Micropore volume (±0.002 cm^3/g)**	**Cumulative pore volume (±0.005 cm^3/g)**
HPT	186	7.8	7.8	0.067	0.456
Ni/HPT	200	9.2	9.6	0.075	0.572
Pt/HPT	187	10.2	9.9	0.066	0.558
Ni/Pt/HPT	191	10.7	10.0	0.069	0.556

Table 2. Calculated band gap energies and rate constant values for the different samples.

Samples	**E_g (eV)**	**k (min^{-1})**
HPT	3.03	0.0027
Ni/HPT	2.54	0.0046
Pt/HPT	2.15	0.0053
Ni/Pt/HPT	2.69	0.0041

Supplementary data. Supplementary data associated with this article can be found, in the online version, at http://dx.doi.org

Author Contributions

The manuscript was written through contributions of all authors. All authors have given approval to the final version of the manuscript.

Notes

The authors declare no competing financial interest.

ACKNOWLEDGMENT

The authors sincerely thank BASF Corporation for kindly supplying the P123 precursor used for TiO_2 synthesis. The *Servei d'Anàlisi Química* and the *Servei de Difracció* from UAB are acknowledged. Financial support from the MAT2011-27380-C02-01, MAT2011-27380-C02-02, MAT2014-57960-C3-1-R and MAT2014-57960-C3-2-R research projects from the Spanish MINECO and the 2014-SGR-1015 project from the Generalitat de Catalunya are also acknowledged. E.P. acknowledges the Spanish *Ministerio de Economía y Competitividad* (MINECO) for the 'Ramon y Cajal' contract (RYC-2012-10839). M. Guerrero acknowledges the support of the Secretary for Universities and Research of the Government of Catalonia and the COFUND Programme of the Marie Curie Actions of the 7th R&D Framework Programme of the European Union for the '*Beatriu de Pinós'* contract (2013 BP-B 00077). S. G. acknowledges "Fondazione Banco di Sardegna" for the financial support.

REFERENCES

[1] M. R. Hoffmann, S. T. Martin, W. Choi, D. W. Bahnemann, Chem. Rev. 95 (1995) 69-96.

[2] C. H. Walker, Organic Pollutants: An Ecotoxicological Perspective, CRC Press (2001).

[3] Y. Wang, C. S. Hong, Water Res. 34 (2000) 2791−2797.

[4] D. Barceló, Emerging Organic Pollutants in Waste Waters and Sludge. Springer, (2005).

[5] E. Forgacs, T. Cserhati, G. Oros, Environ. International. 30 (2004) 953– 971.

[6] C. A. Martínez-Huitle, E. Brillas, Appl. Catal. B: Environ. 87 (2009) 105–145.

[7] C. Martinez, S. Vilarino, M. I. Fernández, J. Faria, L. Canle, J. A. Santaballa, Appl. Catal. B: Envirnon. 142-143 (2013) 633-646.

[8] S. Malato, P. Fernandez-Ibanez, M. I. Maldonado, J. Blanco, W. Gernjak, Catal. Today. 147 (2009) 1–59.

[9] A. O. Ibhadon, P. Fitzpatrick, Catalysts. 3 (2013) 189-218.

[10] J. Schneider, M. Matsuoka, M. Takeuchi, J. Zhang, Y. Horiuchi, M. Anpo, D. W. Bahnemann, Chem. Rev. 114, (2014) 9919−9986.

[11] N. Serpone, J. Phys. Chem. B. 110 (2006) 24287-24293.

[12] N. Nishiyama, Y. Fujiwara, K. Adachi, K. Inumaru, S. Yamazaki, Appl. Catal. B: Environ. in press, http://dx.doi.org/doi:10.1016/j.apcatb.2015.04.015

[13] B. Thirupathi, P. G. Smirniotis, Appl. Catal. B: Environ. 110 (2011) 195-206.

[14] T. Arashi, J. Seo, K. Takanabe, J. Kubota, K. Domen, Catal. Today. 233 (2014) 181–186.

[15] J. J. Murcia, M. C. Hidalgo, J. A. Navío, J. Araña, J. M. Doña-Rodríguez, Appl. Catal. B: Environ. 150-151, (2014) 107-115.

[16] B. D. Fraters, R. Amrollahi, G. Mul, J. Catal. 324 (2015) 119–126.

[17] X. Wang, J. C. Yu, H. Y. Yip, L. Wu, P. K. Wong, S. Y. Lai, Chem. Eur. J. 11 (2005) 2997 – 3004.

[18] S. Shylesh, W. R. Thiel, V. Schunemann, Angew. Chem. Int. Ed. 49 (2010) 3428–3459.

[19] R. A. Young, The Rietveld Method, International Union of Crystallography, Oxford University Press (1995).

[20] D. L. Bish, J. E. Post, Am. Mineral. 78 (1993) 932-940.

[21] K. S. W. Sing, D. H. R. Everett, A. W. Haul, L. Moscou, R. A. Pierotti, J. Rouquerol, T. Siemieniewska, Pure & Appl. Chem. 57 (1985) 603-619.

[22] Y. Liu, M. Aizawa, Z. Wang, H. Hatori, N. Uekawa, H. Kanoh, J. Colloid Interface Sci. 322 (2008) 497–504.

[23] D. A. H. Hanaor, C. C. Sorrell, J. Mater. Sci. Lett. 46 (2011) 855–874.

[24] M. A. Aramendía, V. Borau, J. C. Colmenares, A. Marinas, J. M. Marinas, J. A. Navío, F. J. Urbano, Appl. Catal. B: Environ. 80 (2008) 88–97.

[25] N. Bahadur, R. Pasricha, Govind, S. Chand, R. K. Kotnala, Mater. Chem. Phys. 133 (2012) 471– 479.

[26] B. Rajamannan, S. Mugundan, G. Viruthagiri, N. Shanmugam, R. Gobi, P. Praveen, Acta Mol. Biomol. 128 (2014) 218–224.

[27] B. K. Vijayan, N. M. Dimitrijevic, J. Wu, K. A. Gray, J. Phys. Chem. C. 114 (2010) 21262–21269.

[28] R. M. Mohameda, E. S. Aazama, J. Alloys Compd. 509 (2011) 10132– 10138.

[29] J. M. Thomas, W. J. Thomas, Principles and Practice of Heterogeneous Catalysis, VCH, (1997).

[30] A. Di Paola, G. Marcì, L. Palmisano, M. Schiavello, K. Uosaki, S. Ikeda, B. Ohtani, J. Phys. Chem. B. 103 (2002) 637-645.

[31] E. Masolo, M. Meloni, S. Garroni, G. Mulas, S. Enzo, M. D. Baró, E. Rossinyol, A. Rzeszutek, I. Herrmann-Geppert, M. Pilo, Nanomaterials. 4 (2014) 583-598.

[32] M. Guerrero, A. Altube, E. García-Lecina, E. Rossinyol, M. D. Baró, E. Pellicer, J. Sort, ACS Appl. Mater. Interfaces. 6 (2014) 14583–14589.

[33] S. Wang, J. S. Lian, W. T. Zheng, Q. Jiang, Appl. Surface Sci. 263, (2010) 260-265.

[34] R. López, R. Gómez, J. Sol-Gel Sci. Technol. 61 (2012) 1-7.

[35] G. Sivalingam, K. Nagaveni, M. S. Hegde, G. Madras, Appl. Catal. B: Environ. 45 (2003) 23–38.

[36] Y. Li, X. Li, J. Li, J. Yin, Water Res. 40 (2006) 1119 – 1126.

[37] C. G. da Silva, J. L. Faria, J. Photochem. Photobiol. A: Chem. 155, (2003) 133–143.

[38] N. Zhang, S. Liu, X. Fu, Y. Xu, J. Phys. Chem. C. 115 (2011) 9136–9145.

[39] H. Chen, Y. Ku, Y. Kuo, Water Res. 41 (2007) 2069– 2078.

[40] S. Sakthivel, M. V. Shankar, M. Palanichamy, B. Arabindoo, D. W. Bahnemann, V. Murugesan. WaterRes. 38 (2004) 3001–3008.

[41] X. Liu, Z. Liu, J. Lu, X. Wu, B. Xu, W. Chu. Appl. Surf. Sci. 288 (2014) 513– 517.

[42] R. S. Dhabbe, A. N. Kadam, M. B. Suwarnkar, M. R. Kokate, K. M. Garadkar, J. Mater. Sci.: Mater. Electron. 25 (2014) 3179–3189.

[43] I. M. Arabatzis, T. Stergiopoulos, D. Andreeva, S. Kitova, S. G. Neophytides, P. Falaras, J. Catal. 220 (2003) 127–135.